14.6 CONSTRAINING TEMPERATURE AND HUMIDITY FOR CONVECTION FORECASTING: ON THE NECESSITY OF HAVING SCANNING GROUND-BASED INSTRUMENTS

David Themens and Frédéric Fabry
McGill University, Montreal, Quebec, Canada

ABSTRACT

The ability of different ground-based measurement strategies for constraining thermodynamic variables in the troposphere, particularly at the mesoscale, is investigated. First, a preliminary assessment of the capability of pure vertical sounders for constraining temperature and water vapour fields to current accuracy requirements is presented. Using analyses over one month from the Rapid Refresh model as input to an optimal estimation technique, it is shown that the horizontal density of a network of non-existing ideal vertical profiling instruments must be greater than 30 km in order to achieve accuracies of 0.5 g/kg for water vapour and 0.5 K for temperature. Then, an assessment of a scanning microwave radiometer's capability for retrieving water vapour and temperature fields over mesoscale two- and three-dimensional mesoscale domains is also presented. The information content of an elevation and azimuthal scanning microwave radiometer is assessed using the same optimal estimation framework. Even though, in any specific pointing direction, the scanning radiometer does not provide much information, it is capable of providing considerably more constraints on thermodynamic fields, particularly water vapour, than a near-perfect vertical sounder even using a simple scan pattern. Our findings suggest that measurements from scanning radiometers will be needed to properly constrain the temperature and especially moisture fields to accuracies needed for mesoscale forecasting.

1. CHALLENGE

Weather forecasting is a chaotic process, extremely sensitive to initial conditions. It is thereby crucial that these initial conditions be accurately constrained at appropriate resolutions for the scale of atmospheric phenomena being modeled. Water vapour and temperature are crucial fields to constrain within convection. This is largely due to the strong dependence of convection on the vertical profile of equivalent potential temperature, and thus on the Convective Inhibition (CIN) and Convective Available Potential Energy (CAPE). The sensitivity of convection to thermodynamic properties within the lower atmosphere is highlighted in Crook (1996), Fabry (2006), and Bodine et al. (2010) through their assessments of the impact of thermodynamic properties on CAPE and CIN. Partly as a result of inaccurate initial thermodynamic fields, Quantitative Precipitation Forecasting (QPF) demonstrates relatively low forecast skill during the summer, when convective processes are prevalent (Weckwerth et al. 2004).

Based on the results of Crook (1996), the 1998 NCAR-NOAA Lower Tropospheric Water Vapour Workshop suggested that accuracies of 0.4 g/kg for water vapour and and 1 K temperature were necessary in order to accurately model storm strength and initiation (Weckwerth et al. 1999). In the more recent 2011 Thermodynamic Profiling of the Troposphere (TPT) Workshop, this requirement was relaxed to 1 g/kg and 1 K, respectively, for operational forecast applications (Hardesty et al., 2012), even though vastly different forecast outcomes would occur from a change of humidity and temperature of that magnitude (Crook, 1996).

The horizontal and vertical resolution of these measurements is the next concern. The consensus from the 2011 TPT workshop was that resolutions of 50 to 100 meters in the atmospheric boundary layer (ABL) and ~500 meters above are necessary in the vertical. In the horizontal, resolutions of 200-3000 meters for weather forecasting and less than 20 km for QPF were deemed necessary. Hewison and Gaffard (2006), however, suggest that horizontal resolutions of 1 to 30 km for temperature and 3 to 30 km for water vapour would provide significant benefit for NWP, while resolutions greater than these would provide little further benefit. With respect to time, the 2011 TPT report suggests latencies of no more than 10 minutes for nowcasting applications, while resolutions on the order of tens of minutes to hours would provide adequate benefit (Hardesty et al. 2012).

Meeting these requirements is a major technological challenge. Currently, water vapour and temperature information above the surface is largely limited to coarsely spaced, vertical profiles infrequently measured by radiosondes and commercial airplanes around the world, together with satellite-borne systems. There are, however, a series of potential candidates for implementation in a network conformation (Hardesty et al., 2012): lidar has proven to provide accurate and reliable vertical profiles of water vapour and temperature (Weitkamp 2005); radar refractivity techniques have become well refined, providing a strong constraint on near-surface water vapour and a moderate constraint on near-surface temperature (Fabry et al. 1997; Weckwerth

Corresponding author address: Frédéric Fabry, Dept. of Atmospheric and Oceanic Sciences, McGill University, Montreal, QC, H3A 2K6 Canada; frederic.fabry@mcgill.ca

et al. 2005); infrared radiometers have demonstrated considerable potential for continuous operation retrieval of moderate constraints on water vapour and temperature profiles (Löhnert et al. 2009); and finally, GPS techniques have begun to show promise for providing three dimensional water vapour fields (Bender et al. 2011). Unfortunately, there are drawbacks to each of these techniques that limit their capability to meet the needs outlined above. Lidars and IR radiometers require a cloud-free environment; vertically pointing microwave radiometers and GPS have limited vertical resolution; and radar refractivity is limited to the near-surface. In all cases, as will be shown later, only an extremely dense network of these instruments could possibly provide the needed horizontal resolution and accuracy. In parallel, some satellite techniques may meet these requirements, but do not meet temporal resolution or data latency requirements necessary for observing and forecasting mesoscale phenomena.

Acknowledging these limitations, we shall consider the application of another instrument for providing water vapour and temperature information over three dimensional domains, namely a scanning microwave radiometer. Typically, ground-based microwave radiometers have been limited to vertical profiling and have largely employed scanning under horizontal homogeneity assumptions for the purpose of increasing the information retrievable for vertical profiling within the Planetary Boundary Layer (PBL). In this study, we investigate the potential information available from a narrow-beamwidth, scanning, microwave radiometer over two- and three-dimensional domains in the absence of the horizontal homogeneity assumption. Previous studies of this potential (Padmanabhan et al. 2009, Steinke et al. 2014, Meunier et al. 2014) have been limited to small horizontal domains (typically less than 10km) with a focus on small-scale boundary layer structure, while our interest is towards longer range applications in the mesoscale.

The approach undertaken in this study is theoretical and is rooted in the optimal estimation framework of Rogers (2000). Using this framework, we shall first demonstrate the limitations of a hypothetical, pure-vertical profiling instrument of capabilities well beyond those currently available. We shall then repeat this experiment with a mesoscale-focused radiometer, like the one currently under development at McGill University, and examine the capabilities of such a system for providing three-dimensional water vapour and temperature fields.

2. METHODOLOGY

2.1 Optimal estimation framework[†]

The general purpose of optimal estimation theory is to transform observations of some measurement field, $\boldsymbol{y}$, into a state field, $\boldsymbol{x}$, through the inverse use of a forward model or mapping function, $F(\boldsymbol{x})$. In general, these fields are related through

$$\mathbf{y} = F(\mathbf{x}) \quad (1)$$

In the case of a two-dimensional radiometer retrieval, the measurement field is taken as the brightness temperature measured by a radiometer at the surface and is given by

$$\mathbf{y} = [T_b(f_1,a_1) \ \dots \ T_b(f_N,a_2) \ \ T_b(f_1,a_2) \ \dots \ T_b(f_N,a_2) \ \dots \ T_b(f_N,a_M)], \quad (2)$$

where $T_b(f_n, a_m)$ is the brightness temperature measured at frequency f_n and elevation angle a_m, and N and M are the total number of frequencies and elevations sampled. The state field of interest is composed of the temperature and water vapour mixing ratio arranged in the following manner:

$$\mathbf{x} = \begin{matrix}[T(x_1,z_1) & \dots & T(x_1,z_A) & T(x_2,z_1) & \dots & T(x_2,z_A) & \dots & T(x_B,z_A) \\ w(x_1,z_1) & \dots & w(x_1,z_A) & w(x_2,z_1) & \dots & w(x_2,z_A) & \dots & w(x_B,z_A)]\end{matrix} \quad (3)$$

where $T(x_\beta, z_\alpha)$ and $w(x_\beta, z_\alpha)$ are the temperature and water vapour mixing ratio, respectively, corresponding to the position at horizontal location x_β and vertical location z_α. We may linearize the forward model of (1) to

$$\boldsymbol{y = Kx + \varepsilon,} \quad (4)$$

where $\boldsymbol{K}$ is the linearized forward model, called the sensitivity kernel or forward model Jacobian, and $\boldsymbol{\varepsilon}$ is the measurement error. If we apply Bayes' theorem and assume that the state and measurement vectors follow Gaussian statistics, we may express the most likely retrieved state through the use of the posterior probability distribution. Doing so, the most likely retrieved state $\hat{\boldsymbol{x}}$ can be expressed in terms of an a priori guess $\boldsymbol{x_a}$ and its error covariance field $\boldsymbol{S_a}$

$$\hat{\boldsymbol{x}} = \boldsymbol{x_a} + \boldsymbol{S_a K^T (K S_a K^T + S_\varepsilon)^{-1} (y - K x_a)} \quad (5)$$

where $\boldsymbol{S_\varepsilon}$ is the measurement error covariance matrix (Rodgers 2000). This retrieved state has an associated covariance matrix given by

$$\hat{\boldsymbol{S}} = (\boldsymbol{K^T S_\varepsilon^{-1} K + S_a^{-1}})^{-1}. \quad (6)$$

Within the above retrieval framework resides the capability to assess the information content of a radiometer; for instance, one may calculate the averaging kernel matrix of the instrument $\boldsymbol{A}$, given by

$$\boldsymbol{A} = \hat{\boldsymbol{S}}(\boldsymbol{K^T S_\varepsilon^{-1} K}). \quad (7)$$

The diagonal of the averaging kernel matrix contains information regarding the location and amount of information available within the system, where the individual components of the diagonal can be taken as the number of independent pieces of information associated with a member of the state and its trace can be taken as the total degrees of freedom for signal (DOFs) of the retrieval (Rodgers 2000). The DOFs of the system represent the total number of independent constraints that the instrument provides for constraining the a priori to the actual state. In this study, we will make use of these concepts of information theory to assess the capabilities of a microwave radiometer in undertaking elevation and azimuthal scanning and to

[†] If you are familiar with the Rodgers (2000) approach to estimation theory, jump to Section 2.2.

determine how it fares compared to vertically profiling instruments.

2.2 A Priori

The a priori state of (5), $\boldsymbol{x_a}$, and its associated covariances, $\boldsymbol{S_a}$, have been developed using analyses from the NOAA Rapid Refresh model (RAP). RAP provides hourly, three-dimensional fields of water vapour, pressure, geopotential height, and temperature over the entirety of North America at 13.545 km horizontal resolution and with 50 hybrid levels in the vertical (Benjamin et al. 2004; Bleck et al. 2010).

The a priori state is taken as the monthly-averaged RAP vertical profile of temperature and humidity closest to Montreal, where we have adopted the hybrid coordinate system of RAP for our analysis and capped our retrieval at the 25th hybrid level, corresponding to an upper bound at roughly 300 hPa. This choice of the RAP coordinate system for our analysis allows us to avoid potential correlation artifacts that would result from interpolating to another coordinate system.

The covariances, which will determine how information spreads from measurement locations to surrounding areas, are taken from a monthly climatology assembled from a 500 x 500 km region about Montreal. For its computation, we have assumed horizontally isotropic covariances but have made no assumptions with regards to the vertical structure of the covariance field. The result is a physically plausible covariance error field with respect to a monthly climatology that will serve to describe the uncertainties of the a priori information.

There are, of course, consequences to using a model to generate these covariances in place of actual observations, the most important of which being the tendency for models to smooth out small scale variability, leading to artificially high correlations at these scales. These artificial correlations can produce a non-positive definite covariance matrix. Eigenvalues of the covariance matrix that are zero or negative imply complete a priori knowledge of the state, where components of the state are not linearly independent of one-another (Rodgers 2000).

A lack of positive definiteness in the a priori covariance matrix can lead to poorly normalized solutions or negative components in the DOF components determined using (7). In most applications of model data for generating a priori covariances, positive definiteness is forced by either reducing the number of elements within the state vector or by modifying the covariances in a physically consistent manner. In the event of using a positive semi-definite covariance matrix (i.e., one where all eigenvalues are positive, but very small or zero-value eigenvalues exist), poor normalization or negative DOF components will occur if the instrument retrieval information forces the use of these small eigenvalues. Simply put, the use of a positive semi-definite covariance matrix can generate negative DOF components if the instrument scan pattern is dense enough to force the use of the small eigenvalues of the a priori covariance matrix.

In our case, artificial correlations at small scales can be identified by a “bite out” in the horizontal structure of the covariance field at and below the lowest three grid scales of the model. This is demonstrated in Fig. 1, where we have plotted the horizontal structure of the RAP-generated a priori covariances at the 8th hybrid level. Ideally this plot would demonstrate exponential-like behavior but, as can be clearly seen, there is an obvious departure from this behavior at small scales.

To correct for this “bite out”, we have removed the lowest three horizontal grid scales (scales at or below 40.635 km) from the covariance field and fit the remaining horizontal structure to a double Gauss-Markov model. This fit is then used to extrapolate the covariances for scales smaller than or equal to 40.635 km. An example of this fit is also presented in Fig. 1.

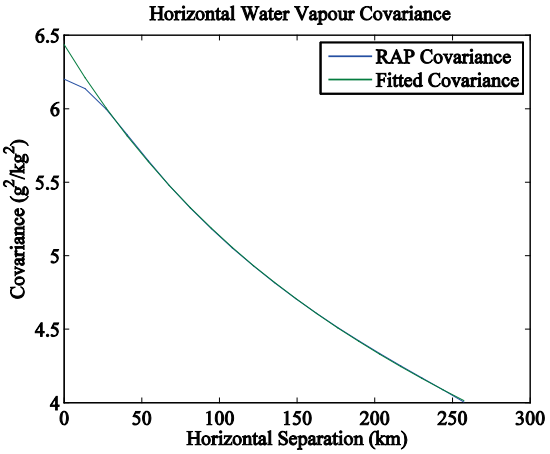

FIG. 1: Horizontal structure of the water vapour covariances at the 8th hybrid level for July, 2011. Those generated by RAP are plotted in blue. The fitted double Gauss-Markov function is plotted in green. The two curves only differ markedly for distances smaller than 40 km

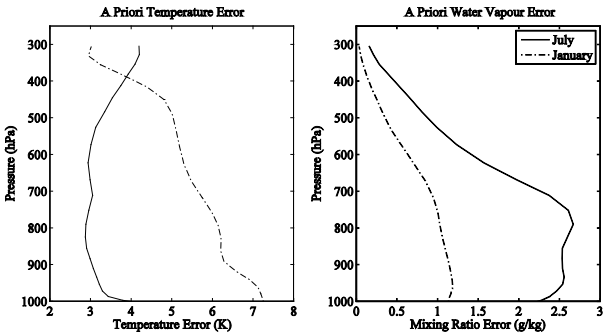

FIG. 2: Water vapour and temperature standard deviations of the a priori for July (solid line) and January (dashed).

For the vertical, a priori covariances are largely anisotropic and a simple method does not exist for identifying the amount of small scale smoothing within the model; as such, we have not modified the vertical

structure of the RAP-generated covariance matrix. This should not be a large issue, as microwave radiometers generally provide low-resolution information in the vertical and thus the smallest vertical scales of the a priori covariance matrix will likely not be used in our application.

The standard deviation profiles for both temperature and water vapour for the periods evaluated in this study are presented in Fig. 2.

3. CAN VERTICALLY POINTING INSTRUMENTS MEET CURRENT NEEDS?

Using this framework, we shall first perform a quick thought experiment. Let us consider a Hypothetical Vertical Profiling Instrument (HVPI) that is capable of retrieving water vapour and temperature at each vertical grid level, at accuracies of 0.1 g/kg and 0.1 K respectively, over the 13.545 km wide column above the instrument, well beyond the specifications of any combination of current instruments. Using the above statistical regression framework, we can examine the potential for such a high accuracy vertically pointing instrument to meet the needs specified in Section 1. For the purpose of this experiment, we shall choose the measurement covariances in this section to be completely uncorrelated and assume direct measurements of the water vapour and temperature fields, such that the sensitivity kernel used is made up of unity elements at the location of instrument measurements and zeros-elements elsewhere. Figure 3 demonstrates the retrieved water vapour and temperature error fields, taken as the square root of the diagonal components of the covariance matrix, derived from (6) using the RAP-generated covariance field from July 2011 with instruments separated by 135.45 km, 40.635 km (3-grid point distance), and 27.09 km (2-grid point distance).

One may note that even the 27.09 km separation case does not satisfy the desired 0.4 g/kg accuracy for water vapour within the boundary layer and lower atmosphere. For temperature, however, the specified requirement of 1.0 K is easily met in both the 27.09 and the 40.635 km separation cases; however, accuracies of 0.5 K, desired for some applications, are not guaranteed in any of the presented conformations.

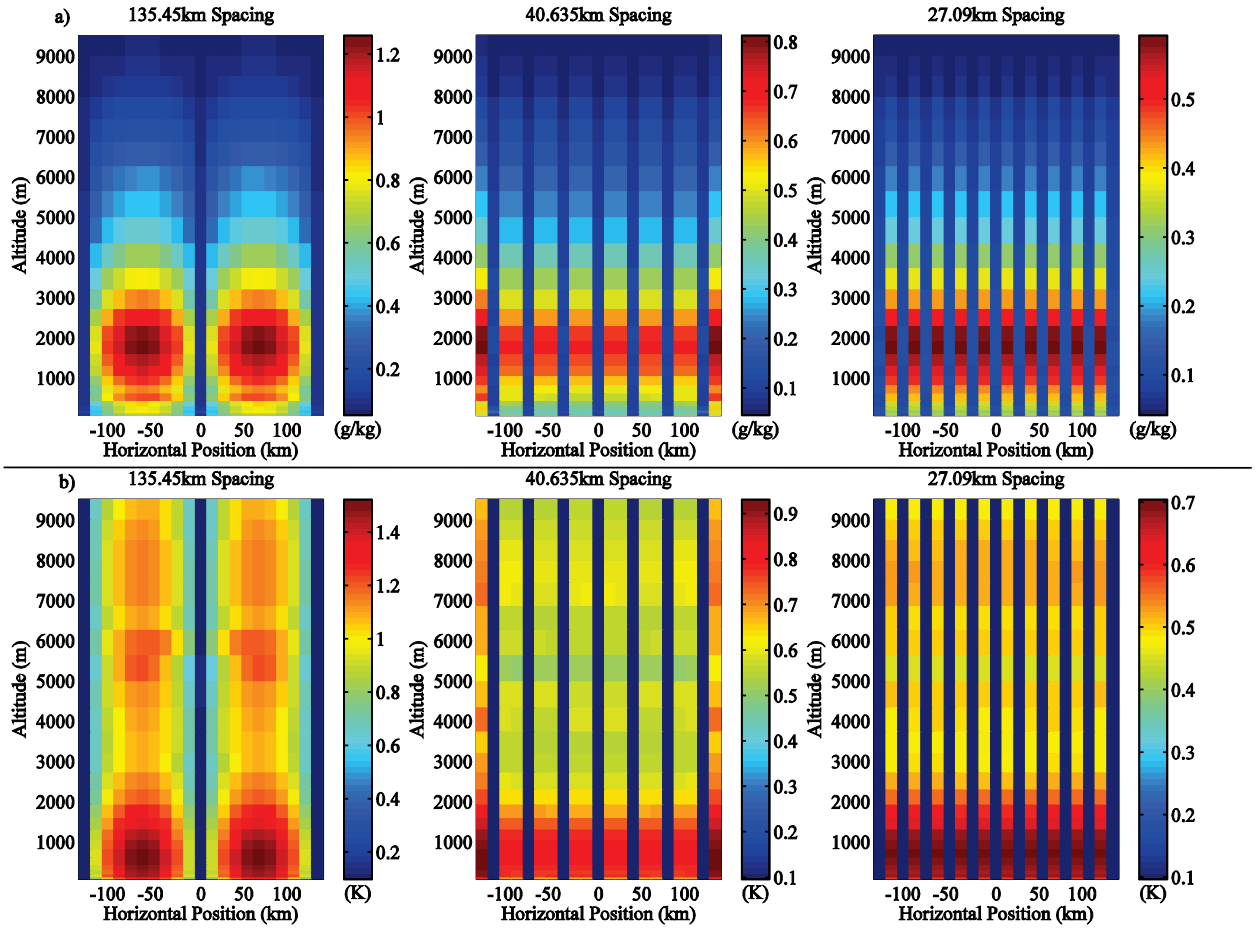

FIG. 3: Water vapour (a) and temperature (b) error fields for HVPI hypothetical profiler instruments networks with 135.45 km, 40.635 km and 27.09 km separation.

In the 2011 TPT workshop, it was proposed that a network of instruments be deployed at a spacing of roughly 100 km to 150 km over the continental United States for the purpose of retrieving temperature and water vapour information at the mesoscale (Hardesty et al., 2012). To illustrate the capability of such a network of vertically pointing instruments, in the case of an idealized hypothetical instrument, one is directed to the 135.45 km spacing results of Fig. 3. While such instruments offer a strong constraint on temperature and water vapour in the vertical above the instrument, the constraint does not spread effectively to neighboring regions, where errors can exceed 1 g/kg and 1 K within roughly 25 km from the instrument. These results illustrate that such a setup would not be capable of sufficiently constraining the local environment to meet our current needs even if we were to deploy vertically pointing instruments with capabilities far exceeding current technologies. They hence stress the need to look at other solutions. We chose to investigate whether scanning instrumentation could meet those needs.

4. THE MESOSCALE RADIOMETER

If we accept the inevitability of having scanning instruments, we must also accept that measurements must be taken up to ranges exceeding 100 km in order for a network deployment to be practical. This rules out any optical or IR-based technology, and, unless we can devise a method to use radar technology to measure temperature and humidity in 3D, forces us to rely on narrow-beam microwave radiometers.

TABLE 1. McGill Mesoscale Radiometer channel parameters

Channel	Frequencies (GHz)				Bandwidth (GHz)
	Cycle 1	Cycle 2	Cycle 3	Cycle 4	
1	16.2	17.4	21.0	22.2	0.2
2	17.0	18.2	21.8	23.0	0.2
3	17.8	19.0	22.6	23.8	0.2
4	18.6	19.8	23.4	24.6	0.2
5	19.4	20.6	24.2	25.4	0.2
6	20.2	21.4	25.0	26.2	0.2
7	22.5				0.4
8	26.5				0.4

For example, the McGill Mesoscale Microwave Radiometer (MMMR) system was designed expressly for scanning applications; as such, frequencies were selected such that it probes a large spread of opacities within the band associated with the 22.235 GHz water vapour line while also maintaining a consistently narrow beamwidth (Fabry and Meunier 2009). A particular difference between this radiometer and other systems available is the use of frequencies below 20 GHz. Most commercially available radiometers were designed with vertical profiling in mind; thus, these radiometers generally focus on channels above 20 GHz that are sufficiently opaque as to provide useful information over the relatively short path travelled by a vertical beam through the troposphere. It is our belief, however, that, in the case of low-elevation scanning, low opacity channels at frequencies below 20 GHz will provide significant information at greater horizontal distances from the receiver. The radiometer's frequencies and bandwidth, in its current conformation, are given in Table 1.

The MMMR system is an eight channel instrument that uses a digitally tuned oscillator to switch across several frequencies. Currently, six of the radiometer's eight channels rotate among four sets of frequencies, each set having six unique frequencies around the 22 GHz water vapour band. The remaining two channels are fixed to frequencies of 22.5 and 26.5 GHz. To insure the capability of scanning at low elevations, the beamwidth is kept relatively constant between roughly 1.4 and 1.7 degrees across all channels. For the purpose of this simulation, we will use the characteristics of the MMMR system to make temperature and humidity retrieval calculations, acknowledging that other narrow-beam radiometers with channels below 20 GHz could demonstrate similar performance.

For our analysis, we have assumed an uncorrelated measurement covariance matrix, where the diagonal elements of the radiometer's measurement covariance matrix are chosen as the theoretical thermal noise errors of a Dicke radiometer given by

$$\sigma_T = \frac{2(T_n+T_b)}{\sqrt{B\tau}} \quad , \tag{8}$$

where T_n is the thermal noise of the instrument, T_b is the measured brightness temperature, B is the channel bandwidth, and τ is the sampling or integration time (Janssen 1993). In our case, we have assumed a $(T_n + T_b)$ factor of 800 K, an integration time of 1/15 seconds, and bandwidths as given in Table 1. This leads to brightness temperature measurement errors of 0.44 K for the varying radiometer channels and of 0.31 K for the fixed channels.

The sensitivity kernel for the radiometer is calculated using a 2D forward model presented in Meunier et al. (2013). This forward model applies the absorption model of Rosenkranz (1998) with an advanced propagation scheme that accounts for both the earth's curvature and beam bending due to variations in the refractive index. It also accounts for both the bandwidth, assuming a square filter band, and beamwidth, assuming a Gaussian beam pattern with suppressed sidelobes. For our purposes, we have only used the bandwidth function of the forward model, so as to limit the computational requirements necessary in calculating the sensitivity kernel. Since the MMMR system has a narrow beamwidth of less than 2 degrees, this assumption should have limited, if not marginal, repercussions on our results (Meunier et al. 2013).

In this study, the sensitivity kernel is estimated using a brute force secant method, where each member of the state vector is independently perturbed above and below the a priori state by 0.5 K (for temperature) or 5% of the a priori (for water vapour). This is done for each channel at each elevation angle.

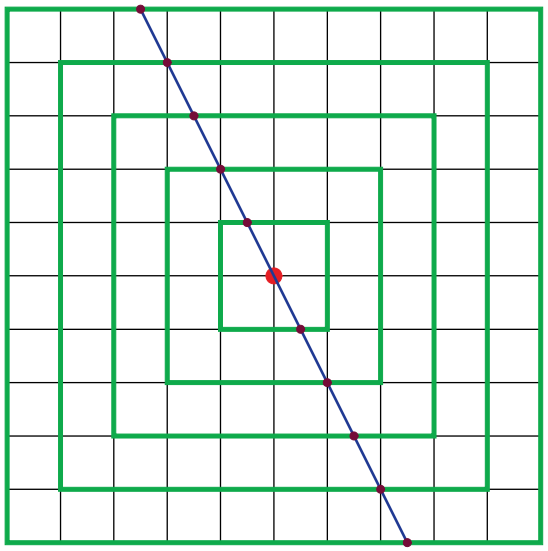

FIG. 4: Diagram of the horizontal grid of the 3D domain with an azimuthal cross section superimposed. The grid rings are drawn in green, the azimuthal cross section is drawn in blue, the radiometer position is drawn in red, and the horizontal grid of the cross section domain is drawn in burgundy.

For 3D retrieval, the process of calculating the sensitivity kernel becomes significantly more difficult. In the 2D case, we may rely on the model's internal interpolation scheme to spread perturbations to the appropriate grid. In the 3D case, we use the above 2D methodology to calculate the sensitivity kernel of 2D cross sections at the desired azimuths through the domain, taking advantage of our use of a horizontally homogeneous a priori state. The horizontal grid spacing of the cross section domain is chosen such that its grid points fall on each ring of points within the 3D domain. This is illustrated in Fig. 4. If the cross section points do not fall directly on the grid points of the 3D domain, the cross section sensitivities are distributed horizontally to the nearest points in that domain within 13.545 km (one grid unit) from the cross section point. This distribution is weighted by the distance between the cross section point and the 3D domain grid points, such that the summed sensitivity is normalized to the original sensitivity of the cross section point. The sensitivity at any point within one grid unit of the 2D cross section points in the 3D domain from a given azimuthal scan is given by the following

$$K_{3D}(x_i) = \left(1 - \frac{d_{i,j}}{\delta}\right) K_{2D}(x'_j), \qquad (9)$$

where K_{2D} is the sensitivity of state point x'_j, $d_{i,j}$ is the horizontal distance between the cross section point (x'_j) and the 3D domain point (x_i), and δ is the grid spacing of the 3D domain.

5. AZIMUTHAL AND ELEVATION SCANNING: WHAT CAN WE RETRIEVE?

Let us now evaluate the information retrievable by the theoretical MMMR system in full azimuth and elevation scanning operation. We shall consider a single case using covariances compiled from July 2011 and assuming a relatively dry, horizontally homogenous a priori state given in Fig. 5. The elevation scan pattern used in this analysis, and those that shall follow, is illustrated in Fig. 6.

Undertaking the procedure outlined in Section 2 with the above considerations, we are able to determine the expected retrieval error and total degrees of freedom retrievable from the dry July environment outlined in red solid lines in Fig. 5 for various azimuthal scan densities. The components of the DOFs for water vapour and temperature are presented in Fig. 7, on various East-West cross sections through the domain using an azimuthal scan density of five degrees.

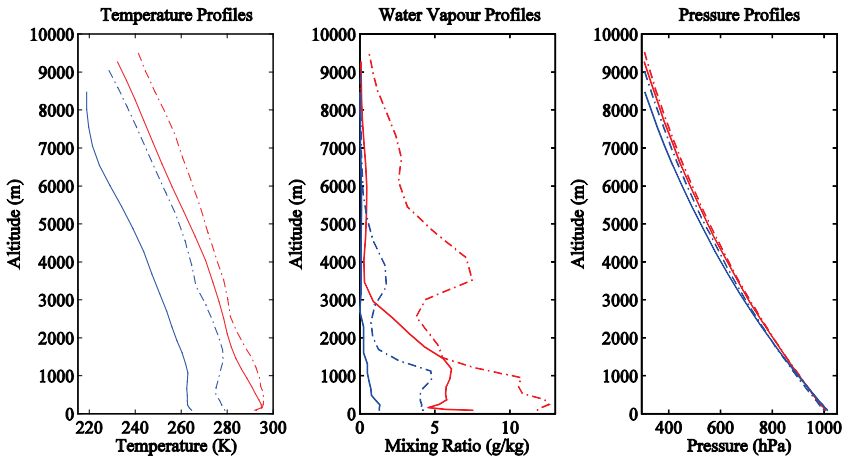

FIG. 5: Water vapour, temperature, and pressure profiles for a relatively dry winter environment at 15 UTC on January 19th, 2012 (solid blue curves), a relatively wet winter environment at 15 UTC on January 1st, 2012 (dashed blue curves), a relatively dry summer environment at 01 UTC on July 1st, 2011 (solid red curves), and a relatively wet summer environment at 17 UTC on July 10th, 2011 (dashed red curves).

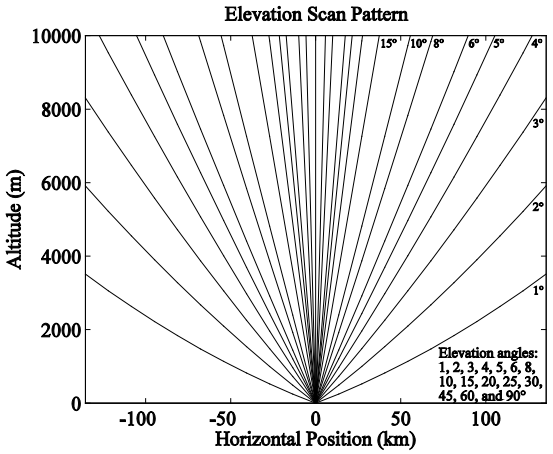

FIG. 6: Elevation scan pattern used in this study.

Overall, at five-degree azimuthal scan density, the system is found to provide 618.0 DOFs for water vapour and 34.8 DOFs for temperature in the dry July environment, well in excess of the roughly 2 to 4 DOFs for each of those parameters found through undertaking scanning for vertical profiling under horizontal homogeneity assumptions (Scheve and Swift 1999, Löhnert et al. 2009). Note that these 15 elevations of 72 azimuths with 1/15 s averaging time for each azimuth-elevation pair could be completed in a couple of minutes by a scanning radiometer, making such a scanning strategy very realizable in a mesoscale forecasting context. As can be seen, the majority of the system's retrievable constraint is restricted to altitudes between 1000 m and 7000 m up to a horizontal radius of roughly 50 km from the instrument, at which distance the low scan density at low elevations results in only discrete rays of information projected from the instrument. A convenient representation of the horizontal distribution of these DOFs, where the DOF components have been summed in the vertical, is presented in Fig. 8.

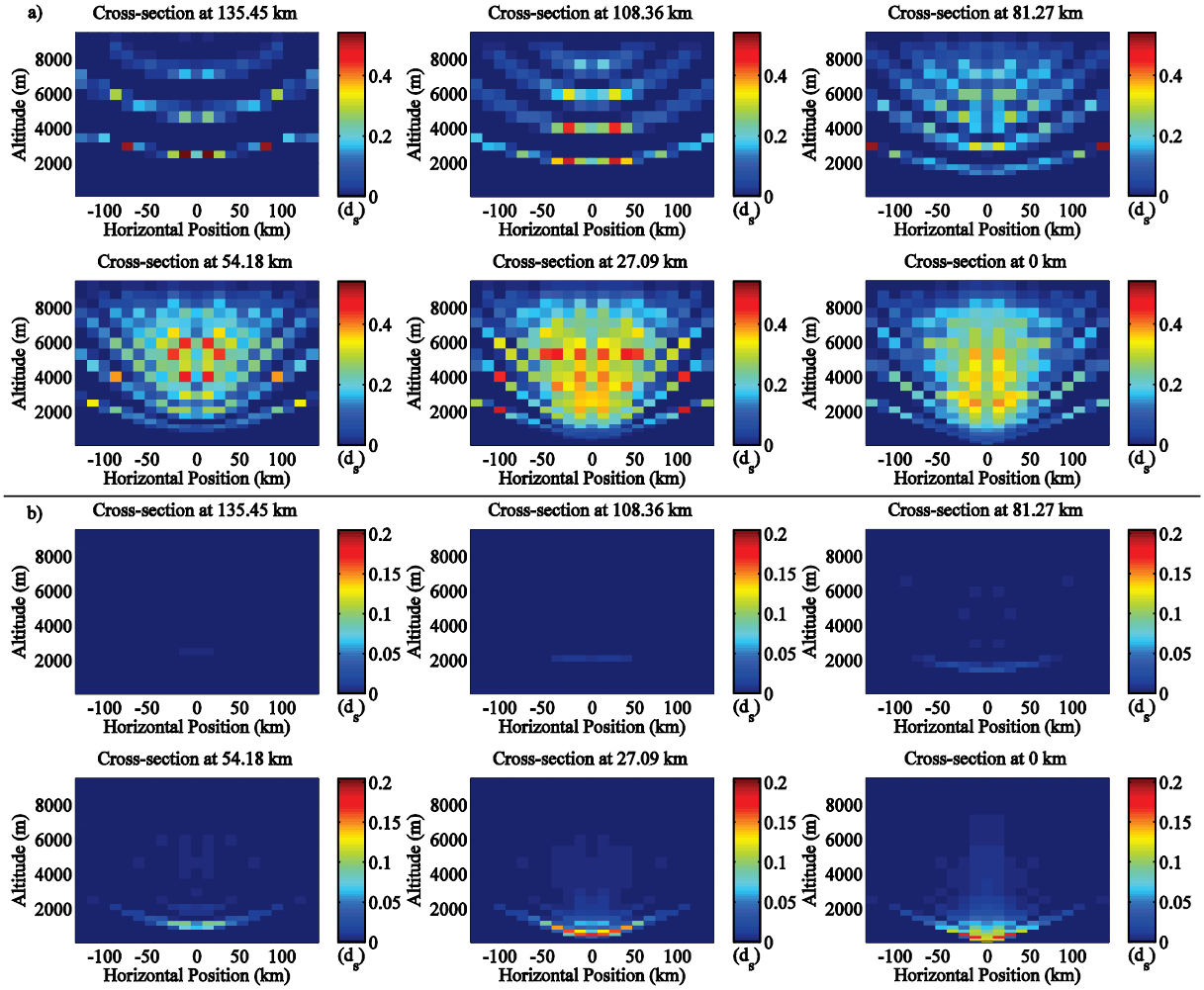

FIG. 7: Water vapour (a) and temperature (b) DOFs retrieved at various east-west cross-sections through the domain for the dry July environment using five degree azimuthal scan density. Cross-section distance south or north from the center of the domain, where the instrument is located, can be found in the label of each plot.

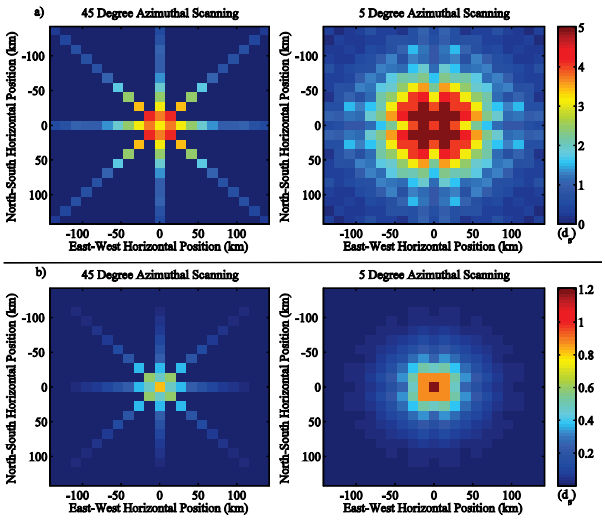

FIG. 8: Vertically-summed water vapour (a) and temperature (b) DOFs at each horizontal position within the specified domain for measurements made every 45° (left) and every 5° (right) in azimuth.

For water vapour, these figures illustrate a local minimum in retrieved information in the column above the instrument followed by a maximum at distances of between one and three grid scales. This suggests that in absence of horizontal homogeneity assumptions, vertically profiling with the MMMR system could in fact be the worst application for such a system. For temperature, results are far less interesting, where vertically summed DOFs simply decrease roughly exponentially from the instrument. This is because the instrument does not make measurements around the 60 GHz band generally used to profile temperature. This procedure has been undertaken for several azimuthal scan densities. The total water vapour and temperature DOFs of these runs are presented in Table 2.

TABLE 2: DOFs for various azimuthal scan patterns

Azimuthal Scan Spacing	Water Vapour DOFs	Temperature DOFs
45°	133.3	12.9
20°	258.1	20.1
15°	326.5	24.0
10°	419.8	26.8
5°	618.0	34.8

Even at scan densities of five degrees, the total information retrieved from the system has yet to saturate. While exploring denser scan patterns could shed light on the point of saturation, time and processing limitations as well as limitations in our chosen a priori covariance fields has limited us to densities greater than or equal to five degrees.

For a conceptualization of these results, we evaluate the expected retrieval errors for the system. We may take the expected retrieval error as the square root of the diagonal entries of the retrieval covariance matrix given by (6). The expected retrieval errors at the same East-West cross sections of Fig. 7 are presented in Fig. 9.

In this simple case, a single MMMR system, situated at the center of the domain, appears to be capable of constraining water vapour to better than ~1.4g/kg accuracy throughout the domain, where errors are largest within the boundary layer at significant distances from the instrument (i.e., in regions not covered by the instrument scan pattern). Within the boundary layer, water vapour errors are projected to remain below 1g/kg within roughly 50km of the instrument, while accuracies approaching 0.7g/kg are achieved directly above the instrument.

For temperature, the results are far less encouraging, where we have little to no constraint on temperature above 1500 meters or beyond 50 km from the instrument. This results in temperature retrieval accuracies of no better than 0.7 K over a small domain. This is, however, a stronger constraint than was initially anticipated, as these frequencies are not typically used for temperature retrieval.

While these results are dependent on the a priori environment and variability, they do demonstrate that the MMMR system could be capable of providing a significant amount of information within summer periods, well in excess of the theoretical maximum of 25 DOFs (one per vertical level) for both water vapour and temperature potentially available from even the most advanced or idealized vertically pointing instruments.

6. NETWORK IMPLEMENTATION OF MMMR SYSTEMS: 2D ELEVATION SCANNING

The capabilities of a single instrument, while interesting, do not highlight the ultimate goal of this exercise, namely the assessment of the capabilities of mesoscale radiometers in a network setting to constrain temperature and humidity fields. In this section, we consider the case of multiple instruments spaced 135.45km apart. Due to the computational and time requirements of the three dimensional retrieval, we shall, from this point on, only consider two-dimensional elevation scanning.

To examine the capabilities of the MMMR system for retrieval within a network of instruments, we conduct a simple experiment, where we have placed three MMMR instruments within the retrieval domain: one at the center of the 270.9 km domain scanning at all elevation angles and the other two instruments at the boundaries of the domain scanning inwards.

For this purpose, we have plotted contours of the temperature and water vapour DOF distributions and their associated retrieval errors for both summer environments in Figs. 10 and 11.

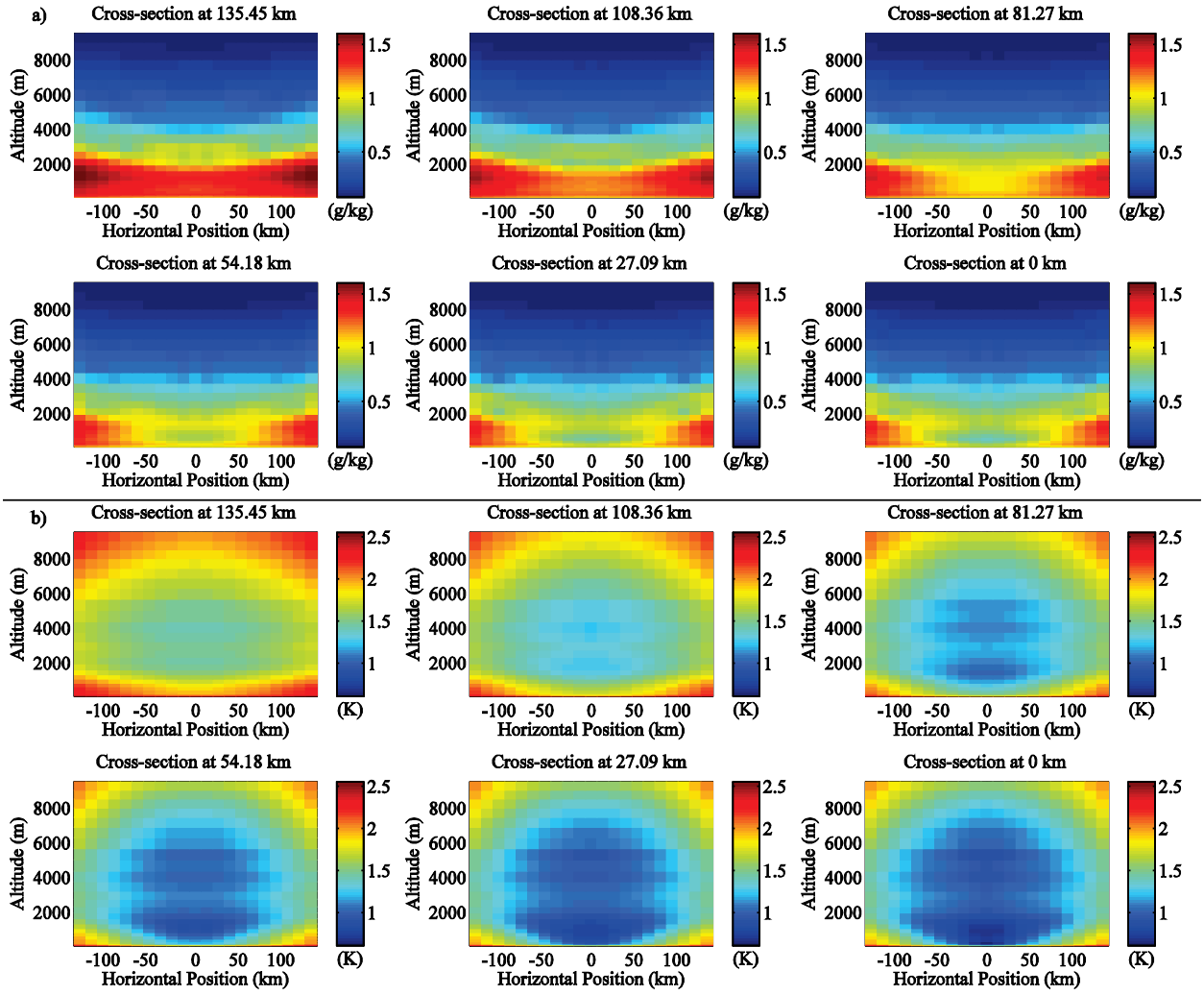

FIG. 9: Water vapour (a) and Temperature (b) errors retrieved at various East-West cross-sections through the domain for the dry July environment using five degree azimuthal scan density. The cross-section distance from the center of the domain is found in the label of each plot.

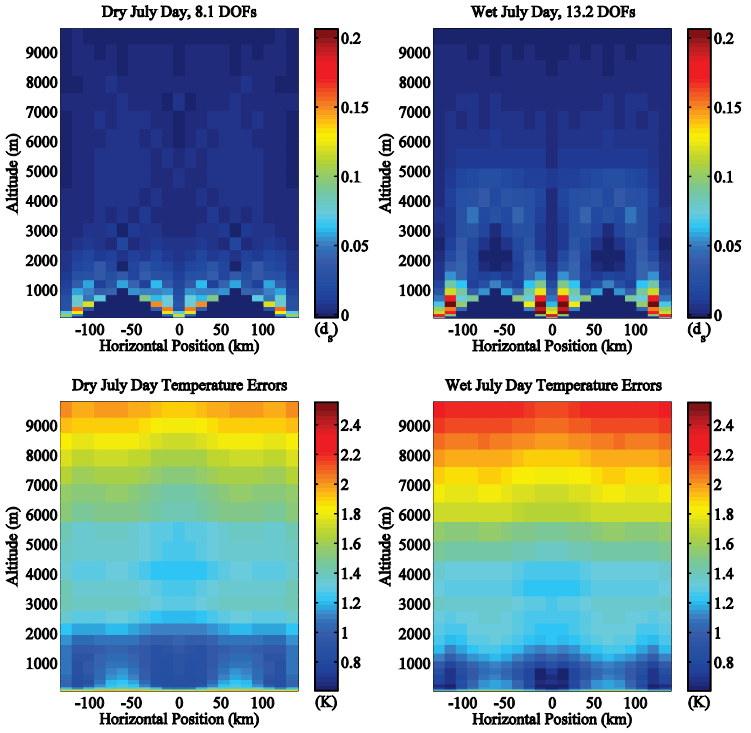

FIG. 10: Temperature DOFs (top) and errors (bottom) for a three-MMMR system conformation for the dry (left) and wet (right) July environments. Total DOFs are listed in the label of the corresponding plots.

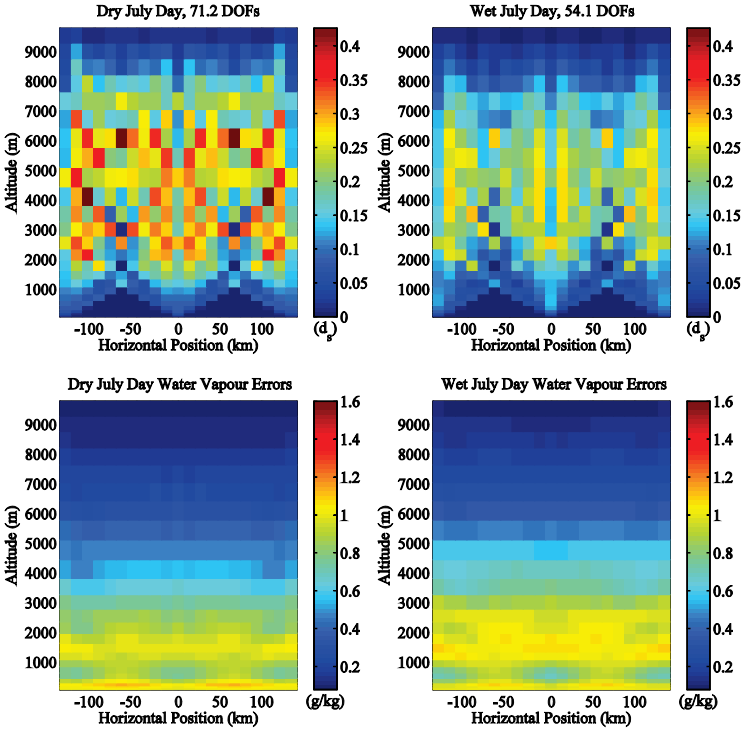

FIG. 11 Water vapour DOFs (top) and errors (bottom) for a three-MMMR system conformation for the dry (left) and wet (right) July environments. Total DOFs are listed in the label of the corresponding plots.

Figures 10 and 11 demonstrate the behavior of the retrievable system information between an extremely dry and a relatively wet July period. Looking at temperature, the temperature weighting functions are highly dependent on the amount of water vapour available within the system: as water vapour increases, the linear independence of the temperature weighting functions also increases, increasing the amount of information that can be retrieved by the instrument. For water vapour, there appears to be a general trend of increasing DOFs with decreasing water vapour. In this case, as water vapour increases, the regions of maximum sensitivity for each channel begin to crowd together closer to the instrument, causing a loss of information as correlations within the field and between channel weighting functions begin to remove what used to be spatially and spectrally uncorrelated information.

The increase in instrument coverage, through adding instruments at the edges of the domain, has filled in the region of little information at the boundaries of the domain and produced a marked area of water vapour information between 1000 and 7000 meters altitude throughout the domain. This addition of instruments at the edges of the domain has led to a significant increase in the constraint on both water vapour and temperature, where water vapour errors are everywhere below 1.1 g/kg, a performance comparable to the errors in humidity obtained with the hypothetical near-perfect vertically pointing instrument simulated in Section 3 given the same instrument spacing (Fig. 3a).

Actually, these 2D simulations underestimate the information obtained by the scanning radiometer and overestimate the errors of the retrievals, particularly at short ranges: The assumption used in 2D retrievals is that we make one set of measurements per elevation angle to constrain the 13.5-km wide “pixels” at different ranges. But in the context of 3D scanning, even at 135 km range, 13.5-km pixels cover six degrees of angle in azimuth, so at far range, more than one azimuth of measurements will constrain those pixels. At close range, it will be even more. For example, let us contrast the cross-section at 0 km of Fig. 9 with the 2D retrievals for the dry July day of Figs. 10 and 11: Even considering the fact that retrievals in Figs 10 and 11 use three instruments, errors at close range are smaller in Fig. 9 with one instrument when we consider the volumetric scanning context. Unfortunately, computing limitations did not allow us to explore the full potential of 3D scanning in a multi-instrument context.

Temperature constraints are, again, not as good, but with the addition of V-band radiometers at each instrument location, we may be able to rectify this initially unsatisfactory result.

7. ADDITION OF A V-BAND RADIOMETER

As can be seen in the previous section, a K-band microwave radiometer is severely lacking in its ability to profile temperature, particularly at altitudes above 1000 meters. A V-band radiometer is designed to operate within the 60 GHz oxygen complex frequency range. Since Oxygen is a well-mixed gas and the 60 GHz oxygen complex is a strong band;,these characteristics make a V-band instrument well suited to profile temperature. In this experiment, we attempt to assess the potential benefit of adding a V-band radiometer to the existing MMMR system. This is done by simply adding a set of V-Band radiometer channels to the initial measurement vector following the specifications of a typical V-Band system. The system chosen for this study is the Radiometrics MP-3000 V-Band radiometer with channels chosen as 51.250, 52.280, 53.855, 54.955, 56.660, 57.290, and 58.800 GHz, following the work of Hewison and Gaffard (2003). The specifications used for the instrument are as given in Liljegren (2002).

The results of implementing this procedure for three instruments in the conformation presented in Section 6 are presented in Figs. 12 and 13, where we have plotted the temperature DOFs and expected retrieval errors for both July experiments.

With the addition of the V-Band radiometer, we achieve both a stronger and better-distributed temperature constraint from the set of instruments, where temperature errors have been reduced significantly in the region closest to the instrument and in the column directly above the radiometer. For both cases, errors of less than 1 K are achieved at all locations below 2000 m altitude. In the regions directly adjacent to the instrument below 1000 m altitude, errors reach as low as 0.3 K. In terms of DOFs, these results are consistent with the previously observed trends, where more water vapour has translated into more temperature information retrieved by the instrument.

While only a small subset of two-dimensional experiments has been presented, the same procedures have been undertaken for several other environments. A summary of the observations from these experiments is presented in Table 3, where two additional environments, namely the dry and wet winter environments of Fig. 5, are presented along with the above July experiment results.

These results attempt to demonstrate the capabilities of the MMMR system at the extremes of each environment in hopes of providing the reader with an appreciable range with which to interpret our results. At these extremes, a single instrument in a 2D setting, undertaking elevation scanning, provides between 26.6 and 37.0 water vapour DOFs and between 3.4 and 6.6 temperature DOFs. Considering an operational instrument undertaking both azimuthal and elevation scanning, these results suggest that, even with variability due to changes in the amount of water vapour in the a priori field or a priori variability, a single MMMR system could provide significantly more information than any single, vertically pointing instrument. However, even considering an instrument density of the order of one per 135 km, we are not yet approaching the accuracy goal set in the TPT workshop report, at least not in the

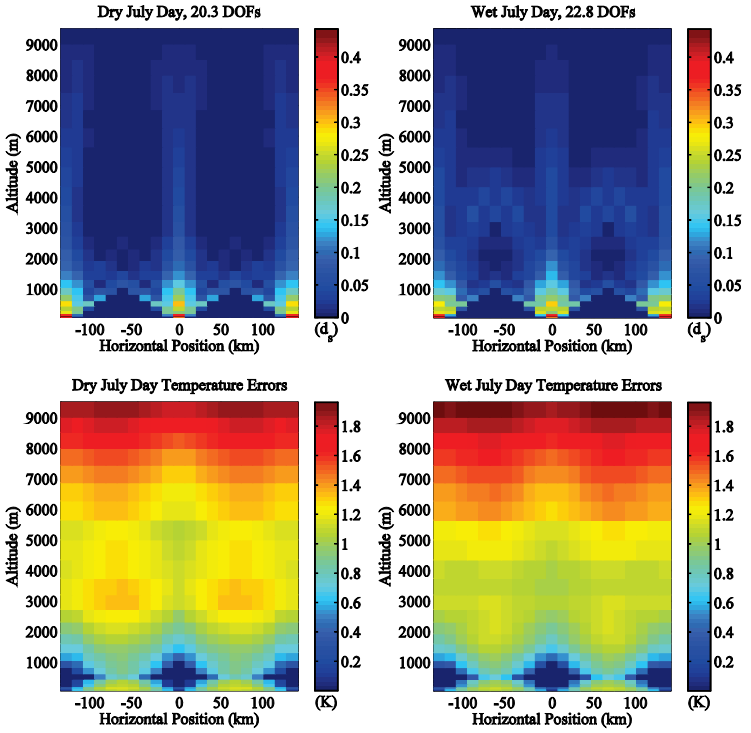

FIG. 12: Temperature DOFs (top) and errors (bottom) for a three-MMMR and three-V-band radiometer conformation for the dry (left) and wet (right) July environments. Total DOFs are listed in the label of the corresponding plots.

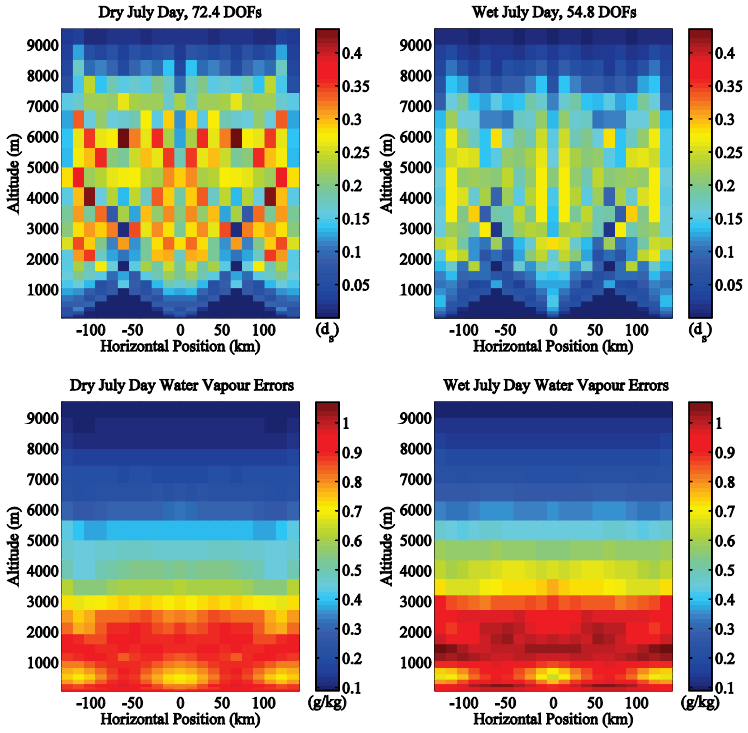

FIG. 13: Water Vapour DOFs (top) and errors (bottom) for a three-MMMR and three-V-band radiometer conformation for the dry (left) and wet (right) July environments. Total DOFs are listed in the label of the corresponding plots.

TABLE 3: Water vapour (WV) and temperature (T) DOFs for various system configurations

Environment	K-Band Radiometer		K-V Band Radiometer		Three K-Band		Three K-V Band	
	WV DOFs	T DOFs	WV DOFs	T DOFs	WV DOFs	T DOFs	WV DOFs	T DOFs
July Dry	37.0	4.1	37.3	9.2	71.3	8.2	72.4	20.3
July Wet	27.3	6.6	27.6	10.5	54.1	13.2	54.8	22.8
January Dry	29.5	3.4	29.6	9.0	58.0	5.7	N/A	N/A
January Wet	26.6	4.4	26.7	9.7	51.5	8.5	N/A	N/A

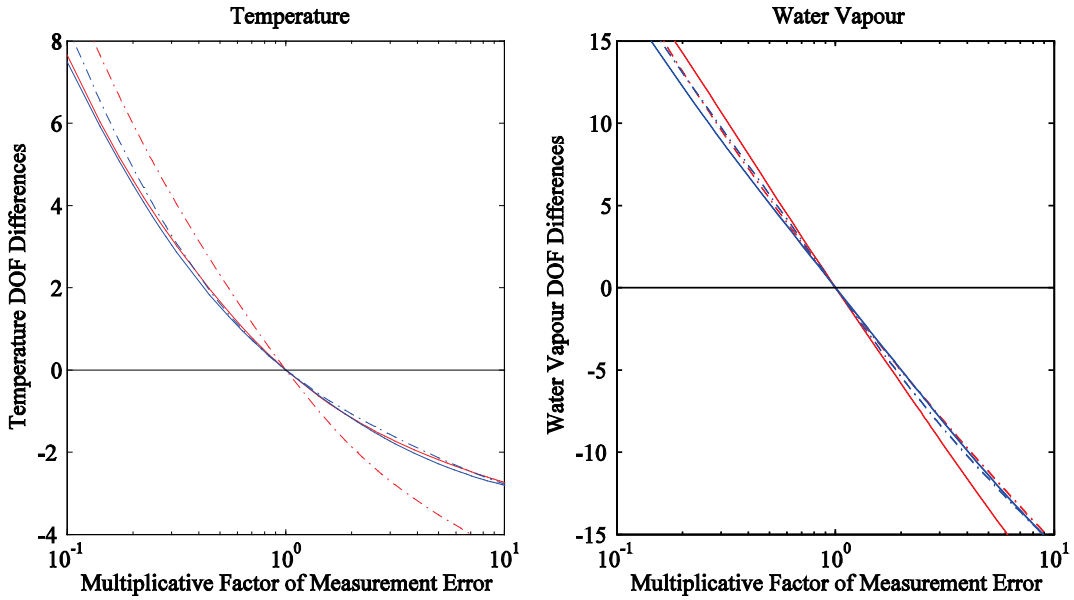

FIG. 14: Differences between the total temperature (left) and water vapour (right) DOFs retrieved by a single MMMR system using the measurement errors of Section 4 multiplied by various multiplicative factors and those determined with no modification for the four July (red) and January (blue) dry (solid) and wet (dash-dotted) cases. Negative values imply a decrease and positive values imply an increase in DOFs from those of the unmodified case.

context of a one-time retrieval using a monthly climatology as a priori knowledge. Better results for all experiments should be expected given a better a priori and by considering repeated measurements every few minutes, but in the absence of knowledge on both the typical magnitude and especially the correlation structure of temperature and humidity errors from analyses made within a weather forecasting context, we could not investigate this possibility.

8. SENSITIVITY TO SYSTEM MEASUREMENT ERRORS

While this study is largely a proof of concept, it is important to determine how sensitive our results are to changes in measurement errors, as the final implementation of this instrument will likely involve the use of further refinements to the instrument design.

To assess the sensitivity of the total information retrieved by the MMMR system to measurement error, we have calculated the 2D water vapour and temperature DOFs retrieved using various multiples of the instrument's previously assumed measurement accuracy. The results of this experiment for all four environmental conditions used previously in this study are presented in Fig. 14, where the difference in the water vapour and temperature DOFs estimated using the standard error set and the modified error sets is plotted against the factor by which the errors have been modified.

As can be seen, a doubling of measurement standard error will lead to a loss of roughly five to six DOFs for water vapour (or about 20%) and between roughly one and two DOFs for temperature, over the entire domain. Likewise, halving the instrument measurement errors results in a corresponding gain in DOFs. The water vapour results appear to be only weakly affected by the environment used, while the temperature results demonstrate a notable departure from the group in the wettest environment. These increases or decreases in the amount of information lead to corresponding changes in the retrieval accuracy; as such, the change in layer-mean water vapour and temperature errors with respect to changes in measurement accuracy are presented in Figs. 15 and 16.

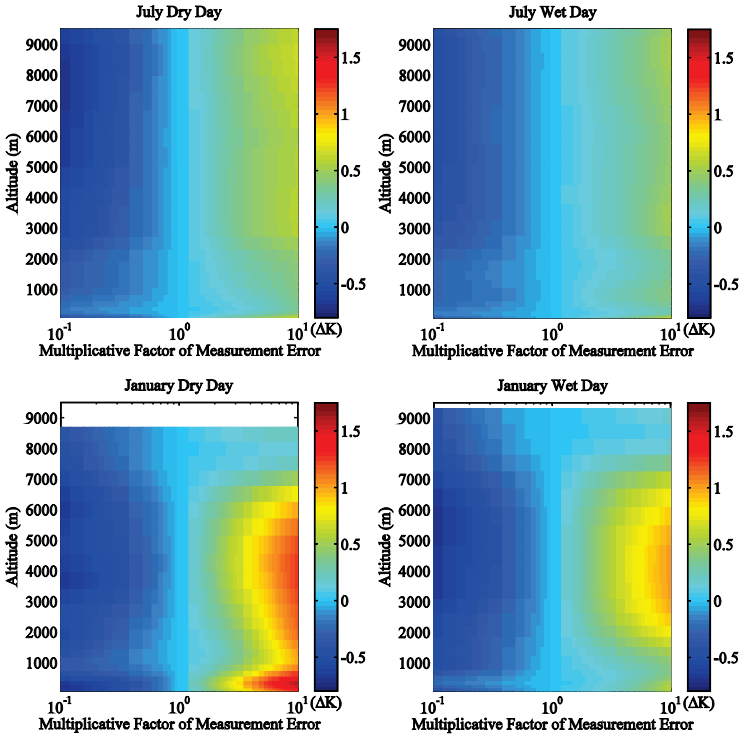

FIG. 15: Differences between the layer-averaged temperature retrieval errors calculated using the measurement errors of Section 4 multiplied by various multiplicative factors and those determined with no modification for the four July (top) and January (bottom) dry (left) and wet (right) cases. Negative values imply a decrease and positive values imply an increase in retrieval errors from those of the unmodified case.

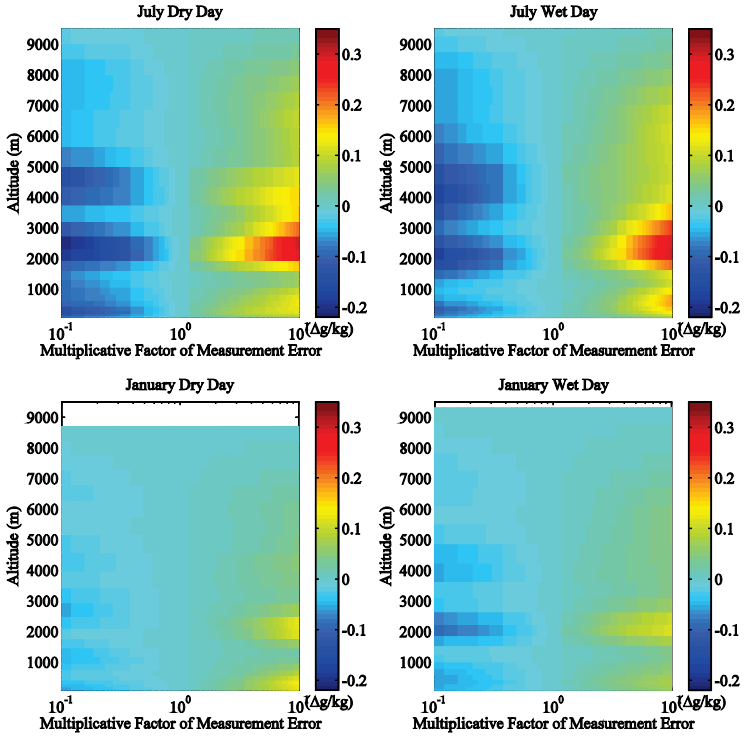

FIG. 16: Same as Fig. 15, except for water vapour.

Looking at the water vapour contours of Fig. 16, we see that there is little improvement in layer-averaged retrieval errors with even a factor three decrease in brightness temperature errors, but the improvement that is achieved is located in the lower part of the atmosphere, where we have the greatest difficulty in constraining water vapour. For temperature, as shown in Fig. 15, an increase in measurement accuracy by a factor three does produce an appreciable increase in retrieval accuracy, particularly in dry environments. Also, these results demonstrate that a significant improvement in measurement accuracy might facilitate the retrieval of temperature at higher altitudes, where the maximum altitude of improvement is highly dependent on the humidity of the environment. This is an encouraging observation and will be investigated more thoroughly in the future to assess the limits of the temperature information retrievable by a microwave radiometer.

9. CONCLUSIONS

This study encompasses a variety of topics addressing the capability of a scanning microwave radiometer for providing accurate, three-dimensional water vapour and temperature fields. Theoretical experiments, run in four different atmospheric conditions, examine the 2D and 3D information content of a scanning microwave radiometer. These experiments demonstrate appreciable retrievable information at distances exceeding 150 km from the instrument. Water vapour information is found to reside primarily in the region between 1000 and 7000 m altitude and temperature information is found to reside much closer to the instrument, largely at altitudes below 1500 m.

For the 3D case of five-degree azimuthal scan density in a dry summer environment, vertically summed water vapour DOFs are found to exceed three DOFs at all locations within 50 km of the instrument, comparable to the 2-4 DOFs for each water vapour and temperature retrievable by a vertically pointing radiometer or a scanning radiometer employing a horizontal homogeneity assumption. Other experiments were undertaken using various conformations of instruments and adding further systems in a 2D elevation scanning setup. Even with the worst case a priori constraint (climatology), we are able to constrain temperature to within ~1 K at all locations below 2000 m and water vapour to accuracies of ~1 g/kg over the entire domain in both summer cases, with accuracies increasing to 0.2 K and 0.7 g/kg, respectively, as one approaches the region just above the instruments. These results are comparable in accuracy to what would be obtained by retrieving temperature and humidity using measurements from a network of non-existing near-perfect thermodynamic profilers spaced every 135 km.

While a radiometer does not appear to be capable of meeting the accuracy requirements of 0.4 g/kg and 1 K needed for mesoscale forecasting without the addition of significant constraints on the a priori state, it provides unique 3D coverage. It is thus likely that a network developed for the purpose of improving mesoscale observations will need to include a combination of radiometers, capable of providing information over large horizontal scales, and vertically pointing instruments, capable of providing high accuracy, high resolution vertical observations at a single location. In addition, more constraints near the surface, inaccessible by either of these systems, is clearly needed.

REFERENCES

Bender, M., G. Dick, M. Ge, Z. Deng, J. Wickert, H. Kahle, A. Raabe, and G. Tetzlaff, 2011: Development of a GNSS water vapour tomography system using algebraic reconstruction techniques, *Advances in Space Research*, **47**(10), 1704-1720.

Benjamin, S.G., D. Devenyi, S.S. Weygandt, K.J. Brundage, J.M. Brown, G.A. Grell, D. Kim, B.E. Schwartz, T.G. Smirnova, T.L. Smith, and G.S. Manikin, 2004: An hourly assimilation/forecast cycle: The RUC**.** *Mon. Wea. Rev*., **132**, 495–518.

Bleck, R., S.G. Benjamin, J.-L. Lee, and A.E. MacDonald, 2010: On the use of an adaptive, hybrid-isentropic vertical coordinate in global atmospheric modeling. *Mon. Wea. Rev.*, **138**, 2188 - 2210.

Bodine, D., P.L. Heinselman, B.L. Cheong, R.D. Palmer, and D. Michaud, 2010: A case study on the impact of moisture variability on convection initiation using radar refractivity retrievals, *J. Applied Meteor. Clim.*, **49**(8), 1766-1778.

Crook, N.A., 1996: Sensitivity of moist convection forced by boundary layer processes to low-level thermodynamic fields. *Mon. Wea. Rev*., **124**, 1767–1785

Fabry, F., C. Frush, I. Zawadzki, and A. Kilambi, 1997: On the extraction of near-surface index of refraction using radar phase measurements from ground targets. *J. Atmos. Oceanic Tech.*, **14**(4), 978-987.

Fabry, F., 2006: The spatial structure of moisture near the surface: Project-long characterization. *Mon. Wea. Rev.*, **134**, 79-91.

Fabry. F., and V. Meunier, 2009: Conceptualisation and design of a "mesoscale radiometer". Proceedings, 8th International Symposium on Tropospheric Profiling, Delft, Netherlands, 18-22 October 2009, paper S06-P03.

Hardesty,R., R. Hoff, F. Carr, T. Weckwerth, S. Koch, A. Benedetti, S. Crewell, D. Cimini, D. Turner, W. Feltz, B. Demoz, V. Wulfmeyer, D. Sisterson, T. Ackerman, F. Fabry, K. Knupp, R. Carbone and R. Serafin, 2011: Thermodynamic Profiling Technologies Workshop**,** *NSF/NWS Workshop Report*.

Hewison, T.J., and C.Gaffard, 2003: Radiometrics MP3000 Microwave Radiometer Performance Assessment, Met

Office, Observations/Development, *Technical Report TR29*, Available from National Meteorological Library, UK.

Hewison, T.J., and C. Gaffard, 2006: Combining data from ground-based microwave radiometers and other instruments in temperature and humidity profile retrievals. WMO Technical Conference on Meteorological and Environmental Instruments and Methods of Observation, (TECO-2006), Geneva, Switzerland, 4-6 Dec 2006.

Janssen, M.A., 1993: *Atmospheric Remote Sensing by Microwave Radiometry*. John Wiley & Sons, Inc, New York,.

Liljegren, J. C., 2002: *Microwave Radiometer Profiler Handbook: Evaluation of a New Multi-Frequency Microwave Radiometer for Measuring the Vertical Distribution of Temperature, Water Vapor, and Cloud Liquid Water.* DOE Atmospheric Radiation Measurement (ARM) Program, Argonne National Lab., Argonne, IL, USA.

Löhnert, U., D.D. Turner, and S. Crewell, 2009: Ground-based temperature and humidity profiling using spectral infrared and microwave observations: Part I. Simulated retrieval performance in clear-sky conditions. *J. Appl. Meteor. Climatol.*, **48**, 1017 - 1032, doi: 10.1175/2008JAMC2060.1.

Meunier, V., U. Löhnert, P. Kollias, and S. Crewell, 2013: Biases caused by the instrument bandwidth and beamwidth on simulated brightness temperature measurements from scanning microwave radiometers. *Atmos. Meas. Tech.*, **6**, 1171–1187.

Meunier, V., D.D. Turner, and P. Kollias, 2014: Tomographic retrieval of a 2D water vapor field by ground-based microwave radiometry. Part 1: Performance simulation. *J. Atmos. Oceanic Tech.*, **31**, in press.

Padmanabhan, S., S.C. Reising, J. Vivekanandan, and F. Iturbide-Sanchez, 2009: Retrieval of atmospheric water vapor density with fine spatial resolution using three-dimensional tomographic inversion of microwave brightness temperatures measured by a network of scanning compact radiometers, *IEEE Trans. Geosci. Remote Sensing*, **47**(11), 3708 - 3721.

Rodgers, C.D., 2000: *Inverse Methods for Atmospheric Sounding: Theory and Practice*, World Scientific.

Rosenkranz, P. W., 1998: Water vapor microwave continuum absorption: a comparison of measurements and models, *Radio Sci.*, **33**, 919 - 928.

Scheve, T.M., and C.T. Swift, 1999: Profiling atmospheric water vapor with a K-band spectral radiometer. *IEEE Trans. Geosci. Remote Sensing*, **37**, 1719–1729.

Steinke, S., U. Löhnert, S. Crewell, and S. Lui, 2014: Water vapor tomography with two microwave radiometers. *IEEE Geosci. Remote Sens. Letters*, **11**, 419-423.

Weckwerth, T.M., V. Wulfmeyer, R.M. Wakimoto, R.M. Hardesty, J.W. Wilson, and R.M. Banta, 1999: NCAR-NOAA lower tropospheric water vapor workshop. *Bull. Amer. Meteor. Soc.*, **80**, 2339–2357.

Weckwerth, T.M., D.B. Parsons, S.E. Koch, J.A. Moore, M.A. LeMone, B.B. Demoz, C. Flamant, B. Geerts, J. Wang, and W.F. Feltz, 2004: An overview of the International H2O Project (IHOP_2002) and some preliminary highlights. *Bull. Amer. Meteor. Soc.*, **85**, 253–277, doi: 10.1175/BAMS-85-2-253.

Weckwerth, T. M., C. R. Pettet, F. Fabry, S. J. Park, M. A. LeMone, and J.W.Wilson, 2005: Radar refractivity retrieval: Validation and application to short-term forecasting. *J. Appl. Meteor.*, **44**, 285 - 300.

Weitkamp, C., 2005: *LIDAR: Range-Resolved Optical Remote Sensing of the Atmosphere*. Springer Series in Optical Sciences.